PAPER • OPEN ACCESS

Traceable x-ray focal spot reconstruction by circular edge analysis: from sub-microfocus to mesofocus

To cite this article: Benjamin A Bircher *et al* 2022 *Meas. Sci. Technol.* **33** 074005

View the article online for updates and enhancements.

Traceable x-ray focal spot reconstruction by circular edge analysis: from sub-microfocus to mesofocus

Benjamin A Bircher[1,3,*] ⓘ**, Felix Meli**[1,3,*] ⓘ**, Alain Küng**[1,*] **and Andrii Sofiienko**[2]

[1] Federal Institute of Metrology METAS, Laboratory for Length, Nano- and Microtechnology, Bern-Wabern, Switzerland
[2] Excillum AB, Kista, Sweden

E-mail: benjamin.bircher@metas.ch, felix.meli@metas.ch and alain.kueng@metas.ch

CrossMark

Abstract

The size and shape of the focal spot, i.e. the area where x-rays are generated in an x-ray tube, is a key figure of merit of a radiographic imaging system, because it governs the achievable resolution and, if the shape is irregular, can introduce anisotropic blur in the radiographs. Size and shape are mainly determined by the diameter of the accelerated electron-beam and electron interactions with the target material. Since focal spot parameters change over time, due to target wear and drift in the electron optics, traceable methods to monitor the focal spot size and shape are required. Here, we present a method to map the 2D intensity distributions of focal spots, ranging from sub-microfocus (0.1 μm) to mesofocus (>50 μm). The method evaluates radial profiles of a circular aperture and applies filtered back projection to reconstruct the focal spot intensity distribution. Special emphasis is placed on traceability and influence factors, such as image noise and aperture geometry. The method was validated over a focal spot range from 0.3 μm to 200 μm. Experimental results were compared to complementary methods, using line pair gauges (JIMA) for microfocus (1 μm–10 μm), e-beam characterisation for sub-microfocus (0.3 μm–1.0 μm), and pinhole camera imaging for mesofocus spots (50 μm–200 μm). Good agreement between the focal spot reconstruction and the complementary methods was achieved. Limitations due to edge penetration, caused by the finite thickness of the circular aperture gauge, were experimentally verified. From these findings, we derived recommendations for an improved gauge geometry, regarding its thickness and the aperture diameters. The method perfectly complements the well-established pinhole imaging, which is limited to focal spots larger than ∼50 μm.

Keywords: x-ray tube, focal spot size, 2D intensity distribution, sub-microfocus (nanofocus), microfocus, mesofocus, filtered back projection

(Some figures may appear in colour only in the online journal)

---

[3] Contributed equally.
[*] Authors to whom any correspondence should be addressed.

1. Introduction

Radiographic and x-ray computed tomography systems, used for non-destructive testing and dimensional measurements, regularly require resolutions in the micrometre range. Traceable measurement methods for determining the focal spot size of high resolution x-ray tubes deliver one of the most important parameter for the attainable resolution [1]. Some methods assess the overall resolution capability of an x-ray imaging system, using wave standards [2–4], grid structures [5, 6], or touching spheres [7]. These take into account the complete computed tomography imaging chain, i.e. consider influences from the focal spot, positioning stability, detector, and reconstruction. Whereas this is an important figure of merit for the complete system, it is sometimes favourable to selectively characterise the focal spot, e.g. for x-ray tube development, optimisation, and condition monitoring.

Since no standard specifies focal spot measurements below 5 μm [8], there is no generally accepted gauge or analysis method. A well-established gauge type is the Japan Inspection Instruments Manufacturers' Association (JIMA) target [9], however, there is no consensus on the analysis [9, 10]. Further suggested gauges include wire gauges, according to EN 12543-5 [9, 10], irregularly spaced line groups [11], and tungsten tips [12]. From the data, either a modulation-transfer function or an integrated line profile of the focal spot perpendicular to the structure's edges can be obtained [8, 10]. This can be used to estimate resolution capability or size parameters, either by setting thresholds (EN 12543-5) or by assuming intensity distributions, usually Gaussian, Lorentzian, or a superposition thereof. However, these methods do not provide the 2D intensity distribution. For this purpose, pinhole cameras are commonly used [13], which are limited to larger spots, as the pinhole should be significantly smaller than the spot size under investigation. Due to manufacturing limitations, the smallest pinholes diameters available are in the range of 10 μm (EN 12543-2). Promising methods for small spots rely on the application of micro-structured gauges. These gauges are typically made of a radiographically transparent substrate, e.g. a thin silicon wafer, and a radiographically opaque structured layer of a high-density material, such as lead, gold or tungsten. To deconvolute the 2D distribution of the spot, the structures should provide edges in all directions. Possible shapes of the structured layers are circular holes [14], converging line group patterns (Siemens star) [15], coded masks [16], and ring patterns [17], which enable the determination of the focal spot distribution by image deconvolution. Furthermore, focal spot distributions were determined by convolutional neural networks, using radiographs of arbitrary structures [18]. For methods using image deconvolution algorithms, noise and filtering posed major challenges [16, 17].

Calibrated features on the used structures can provide direct traceability for the spot size to be determined. Shape irregularities of structures limit the smallest reliably detectable spot size and should, thus, be characterised. These characterisations can become very extensive and cost-intensive for complex shaped structures. Circular apertures (holes gauges) are straightforward to calibrate and provide edges in all directions.

Their application for reconstruction of sub-millimetre focal spot sizes of medical x-ray tubes was demonstrated by di Domenico *et al* [14]. However, the application to micrometre and sub-micrometre focal spots has not yet been demonstrated, because it poses high demands on the quality of the gauges and their calibration. Further, the robustness against noise due to the low x-ray intensity is critical and the lack of standardised methods to compare to challenging. Traceability and influence factors, such as image noise and non-ideal gauge geometry, thus, remain to be investigated.

Here, we present a traceable method to map the 2D intensity distributions of focal spots ranging from about 0.1 μm to 100 μm. Special emphasis is placed on traceability and major influence factors, such as radiographic noise, form deviations of the aperture, and edge penetration effects because of to the finite thickness of the gauge. The method perfectly complements pinhole imaging, which is limited to focal spots above about 50 μm. It was validated on three x-ray tubes generating focal spot sizes from 0.3 μm to 200 μm (full-width at half-maximum (FWHM)) and compared to line pair gauges (JIMA target), pinhole imaging, and focal spot size estimations based on the electron-beam diameter.

2. Method

2.1. X-ray focal spot reconstruction by circular edge analysis

The purpose of the method presented, is to calculate the shape and size of the focal spot of an x-ray source from an image of a small, circular aperture. The spot shape is deduced from edge profiles in all directions using filtered back projection (figure 1). The main principles of the method were introduced by Di Domenico [14]. We implemented it in a program (NI LabVIEW), which performs the following routines: First, based on a manually selected area in the radiograph, the aperture is centred and a region of interest with the size of $2d \times 2d$ (d = diameter of the aperture) is extracted. This is done by the conversion to a binary image (threshold) and using the centre of gravity for the location, and the bright/dark ratio for a first diameter estimation. Second, the edge of the aperture is extracted by thresholding the local derivative of the radiograph. Subsequently, a robust circular fit is used to obtain the location and diameter in pixels (figure 1(a)). For the robust circle fit, outliers are filtered out for further iterations. The effective image pixel size, i.e. magnification $m = \text{SDD/SOD}$ is obtained from the known, calibrated aperture diameter in μm and the fitted diameter in pixels (SDD: source-detector distance, SOD: source-object distance). The focal spot magnification of $m - 1$ is derived from geometric considerations. Third, radial grey value profiles are extracted using bilinear interpolation (figure 1(b)). The number of profiles can be chosen from 4 to 720, with 360 profiles being the default value. The extracted profiles form a sinogram (figure 1(c)), which can be deconvoluted into integrated line profiles of the focal spot by derivation, under the assumption of a perfectly sharp edge (figure 1(d)). As these profiles correspond to a Radon transform of the focal spot in the angular direction parallel to the edge, the arbitrary 2D focal spot intensity distribution can
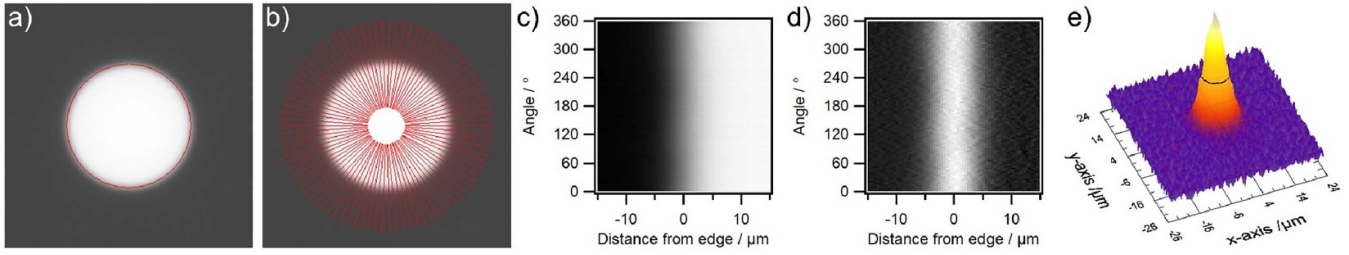
Figure 1. Principle of x-ray focal spot reconstruction from circular edge analysis: (a) A circle is fitted to the radiograph of an aperture of known diameter. (b) Radial profiles are extracted perpendicular to the edge and arranged into a sinogram (c). To deconvolute the focal spot from the edge, the derivative of each profile is calculated (d). A filtered back projection enables the reconstruction of the two-dimensional intensity distribution of the x-ray focal spot (e).

be reconstructed, using filtered back projection [19], i.e. an implementation of the inverse Radon transform (figure 1(e)). To estimate spot size parameters from the 2D intensity distribution, a rotational symmetric Gaussian or a Pseudo-Voigt function is fitted, which is parametrised by a FWHM value. The intended scope of application cover focal spot sizes from about 0.1 μm to 100 μm. The size range is not limited by the method, but rather a consequence of available aperture diameters and influence factors.

2.2. Experimental boundary conditions

The aperture should be a small circular hole, in a thin high-density material. Possible realisations can be found in the experimental section. The diameter should be about five times the expected spot size, and the shape deviations of the aperture should be considerably smaller than the expected focal spot size. A diameter and roundness calibration is recommended and required for traceable measurements. In the following, the boundary conditions of the measurement parameters are explained in more detail.

Depending on the expected focal spot size, an appropriate aperture diameter, magnification and detector size has to be chosen. The first important parameter to select is the required minimum magnification, m, which depends on the expected spot size, a, the desired spot resolution in number of pixels across the spot, n, and the detector pixel pitch, p. Recommended values for n are in the range of 5–20. Realistic values for m will also depend on the reasonably achievable contrast-to-noise ratio, CNR, and the experimental setup, i.e. minimum source-object distance, SOD, and maximum source-detector distance, SDD (m = SDD/SOD).

$$m \geqslant \frac{pn + a}{a} \cong \frac{pn}{a}. \tag{1}$$

The lower limit of the aperture diameter is related to the maximum acceptable curvature of the edge. In [14], a minimum diameter was derived that limited the aperture curvature to below the effective pixel size. This results in elevated minimum diameters that require large fields of view to be imaged. Thus, following the geometrical considerations in [14], we have derived a minimum diameter limit, based on the maximum permissible curvature relative to the focal spot size:

$$d \geqslant a\frac{m-1}{m}\left(T + \frac{1}{4T}\right) \tag{2}$$

with aperture diameter, d, focal spot size, a, magnification, m and the relative tolerance, T, i.e. permissible curvature relative to focal spot size. Simulations revealed that using a tolerance of $T = 5\%$, resulted in focal spot FWHM deviations below 2% and relative RMS shape deviations below 0.25% (section 3). Thus, equation (2) can be simplified to $d > 5a$, i.e. the aperture diameter should be more than five times the focal spot size.

The upper size limit of the aperture diameter is related to the detector size and magnification. The acquired x-ray image should have a size bigger than $2d \times 2d$, where d is the aperture diameter. Therefore, the upper size limit of d is related to the size of the detector, L, or the detector pixel number, N:

$$d < \frac{L}{2m} \cong \frac{aN}{2n}. \tag{3}$$

3. Validation by simulations

The validation of the method is based on the evaluation of simulated images, obtained by the convolution of an aperture with various spot shapes. In a first step, the influence of the number of profiles, the back projection filter, the image resolution and noise was evaluated for a Gaussian spot distribution, the aperture being 20 times larger than the FWHM of the spot. As a rotationally symmetrical Gaussian spot was used, the influence of the number of profiles on the FWHM value was negligible. Within the range of 36–720 profiles, the effect led to relative deviations in FWHM below 10^{-4}. The effect of the applied filter for the filtered back projection depends on the image resolution [20]. Typical filters are Ram-Lak, Shepp-Logan or Hann. Figure 2 shows that low image resolution resulted in overestimated FWHM. The default filter used was Shepp-Logan, as it represents a good compromise between resolution and noise rejection. To resolve a 1 μm spot with 10×10 pixels, an effective pixel size of 0.1 μm is required, which is equivalent to a magnification of 1000× for 100 μm detector pixels. As it might be difficult to realise the required magnifications experimentally, the effect of limited resolution is not negligible. A thin target helps to reduce the minimal SOD and a detector with small pixels requires a lower magnification (equation (1)) to achieve a certain resolution. From figure 2 we recommend to
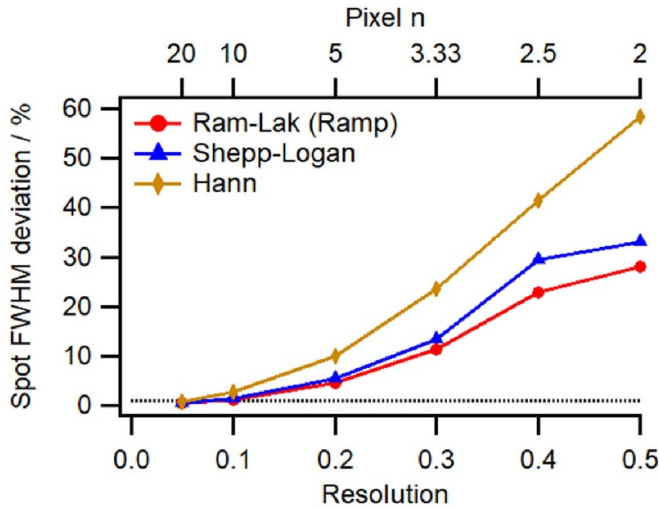
Figure 2. Influence of resolution and filter type on the focal spot size reconstructed by filtered back projection.

resolve focal spots with more than 5 pixels (resolution < 0.2), which is similar to the recommendation in [14] and results in focal spot FWHM deviations below 5%.

The effect of image noise had a severe impact on the quality of the spot intensity distribution (figures 3(a) and (b)), but the effect on the fitted FWHM was far below 1% even for low image CNRs. To quantify the effect of image noise on the focal spot shape, a quality measure was introduced: 1-(relative RMS deviation). As shown in figure 3(c), focal spots resolved with fewer pixels were less prone to image noise. This is explained by the fact that the edge blur is distributed over a smaller range of pixels, resulting in a steeper grey value transition, which is less affected by noise. To obtain an acceptable focal spot quality (⩾95%), the following minimum CNR should be adhered to:

$$\mathrm{CNR} > \frac{1}{2}n^2. \tag{4}$$

With n being the required spot resolution (number of pixels across the spot at FWHM) and CNR according to

$$\mathrm{CNR}_{\mathrm{profile}} = \frac{\mathrm{GV}_{\mathrm{bright}} - \mathrm{GV}_{\mathrm{dark}}}{\sqrt{\frac{1}{2}(\sigma_{\mathrm{bright}}^2 + \sigma_{\mathrm{dark}}^2)}}. \tag{5}$$

This CNR definition is an estimation of the average noise on the extracted edge profiles, described by the averaged standard deviations of the grey values in the free beam, σ_{bright}, and behind the material, σ_{dark}, relative to the change in grey value between the free beam, $\mathrm{GV}_{\mathrm{bright}}$, and behind the material, $\mathrm{GV}_{\mathrm{dark}}$. Thus, it deviates from the CNR definition commonly used for computed tomography data, e.g. [21], as a measure for detail detectability. Increasing CNR can be achieved by longer exposure times or image averaging. Drift corrected image averaging was used to produce high CNR images. Image binning can also increase the CNR, but reduces the spot resolution. Both have a positive effect on the SNR of the spot reconstruction, but binning has the tendency to overestimate the FWHM due to the larger effective pixel size.
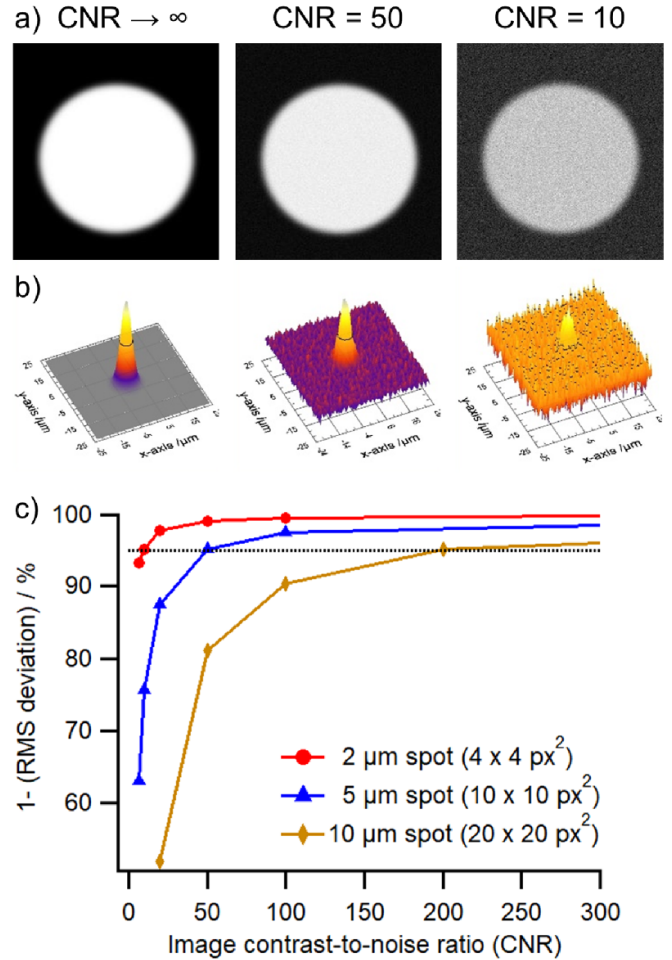

Figure 3. Effect of image noise on the reconstructed focal spot. (a) Simulated apertures (Ø 100 μm) with different contrast-to-noise ratios (CNR) and (b) reconstructed focal spots (FWHM = 5 μm). (c) Quality of the reconstruction in terms of RMS deviation for different number of pixels n across the spot (dashed line: 95% threshold).

Next, the effect of roundness deviations of the circular aperture was simulated. A sinusoidal deviation with various amplitudes and number of undulations (lobes) were introduced. Figures 4(a) and (b) show simulated radiographs and reconstructed focal spots from apertures with no (ideal) and 20% roundness deviation (peak-peak) relative to the focal spot size with 3 and 9 lobes. The effect on the spot shape strongly depended on the number of lobes and if the number was even or odd (figure 4(c)). Interestingly, the determined FWHM was insensitive to the number of lobes (deviations < 0.4% for 2–50 lobes), but strongly depended on the form deviation relative to the focal spot size (figure 4(d)). From this, it is recommended that the form deviation of the aperture should be below 20% of the expected focal spot size, resulting in FWHM deviations below 3 %.

Finally, blur introduced by edge penetration was characterised. It emerges because of the finite thickness of the gauge in combination with the oblique transmission angles, due to the cone-beam arrangement. In order to limit this effect, the transmission angle at the edge of the gauge and the gauge thickness
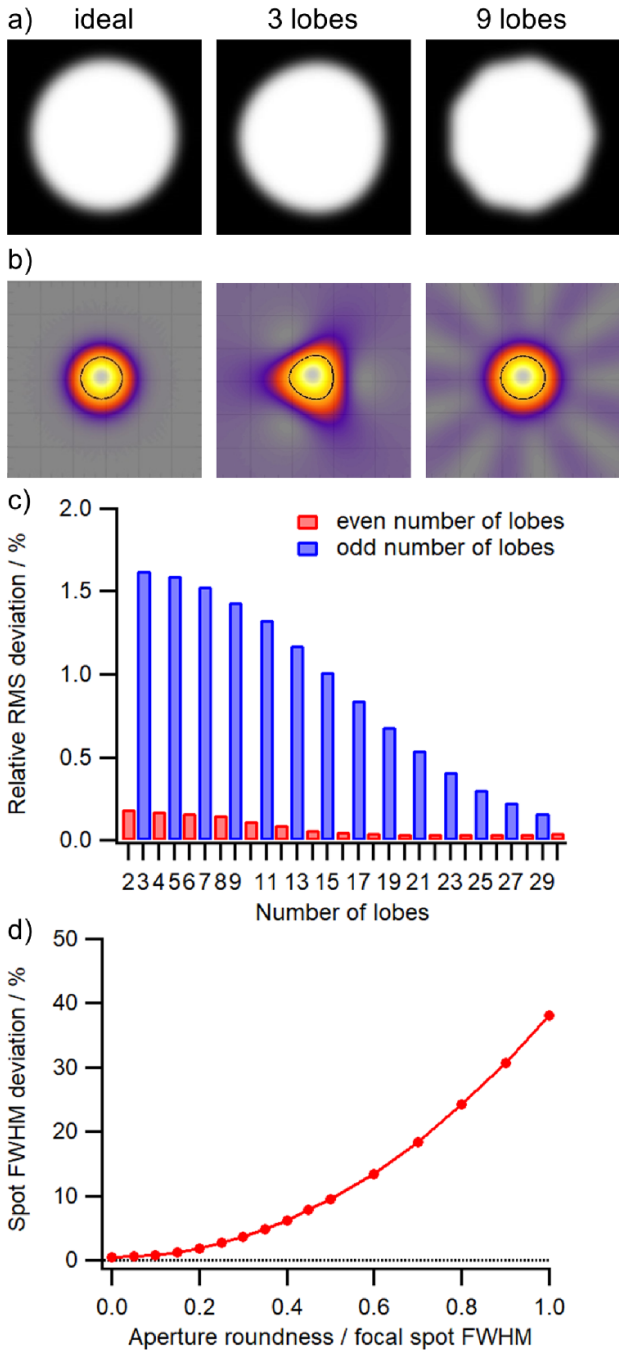
Figure 4. Influence of aperture form deviations on focal spot reconstruction: (a) Apertures with different form deviations (20% of spot size) and (b) reconstructed focal spots. (c) Number of lobes against focal spot shape deviation (form deviation 25% of spot size). (d) Relative form deviation against spot FWHM deviation.

are subject to certain limits, which are subsequently derived. A simple linearised model, based on geometrical considerations, estimates the blur, u, due to edge penetration to be

$$u = \frac{t_{\text{eff}} m d}{2 \, \text{SDD}}. \tag{6}$$

With magnification, m, aperture diameter, d, and source-detector distance, SDD. The effective gauge thickness, t_{eff}, was assumed to be depending on the actual thickness of the
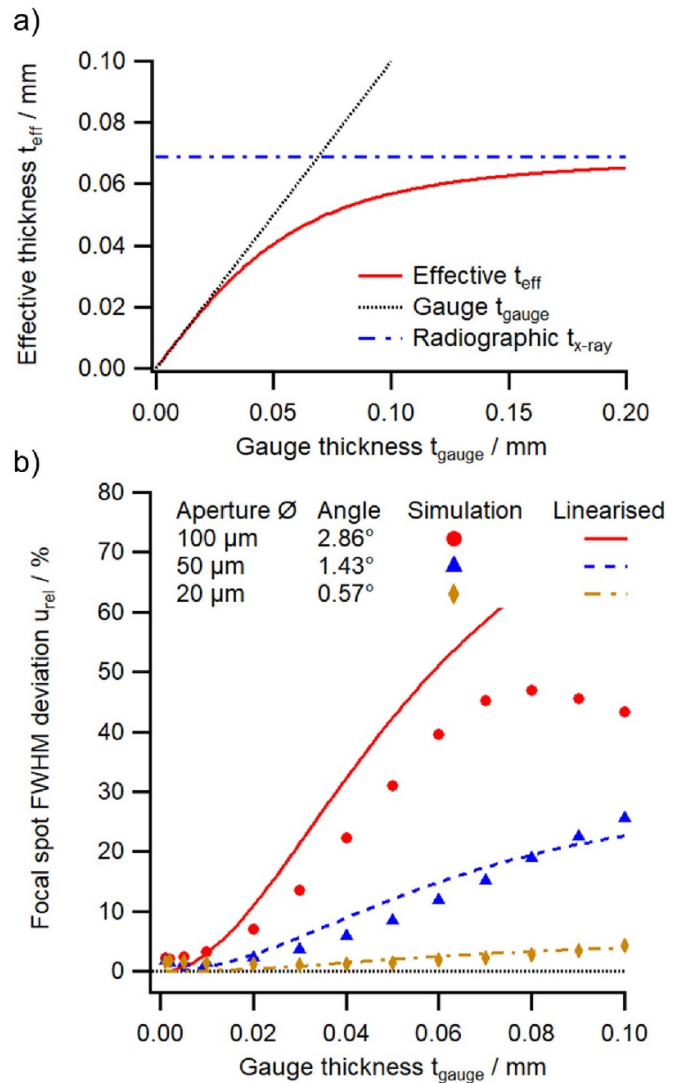

Figure 5. Influence of aperture edge penetration on the focal spot size, governed by the angle of transmission and the gauge thickness. (a) The effective thickness is calculated from the thickness of the gauge material, t_{gauge}, and the radiographic penetration length, $t_{\text{x-ray}}$ (for tungsten carbide at 29.7 keV). (b) Validation of the linearised model: The markers show values derived from radiographic ray-tracing simulations and the lines the linearised model provided in equation (8) for a focal spot size of 2 μm (SOD = 1 mm, SDD = 1000 mm) and different aperture diameters, i.e. transmission angles, and thicknesses.

gauge material, t_{gauge}, for thin gauges, which are completely penetrated by the x-rays, and on the apparent radiographic thickness, $t_{\text{x-ray}}$, i.e. the depth where all relevant radiation is absorbed, for thick gauges. To model this behaviour, the effective thickness was calculated as the harmonic mean of the magnitude of the gauge and the radiographic thicknesses as shown in figure 5(a):

$$t_{\text{eff}} = \left(\frac{1}{t_{\text{gauge}}^2} + \frac{1}{t_{\text{x-ray}}^2} \right)^{-\frac{1}{2}}. \tag{7}$$

To establish appropriate values for $t_{\text{x-ray}}$ and validate the linearised edge penetration model, radiographic ray-tracing

Table 1. Experimental setups to compare the focal spot reconstruction from a circular aperture to complementary methods for focal spot sizes ranging from 0.3 to 200 μm (FWHM).

	Setup	Microfocus (4.1)	Sub-microfocus (4.2)	Mesofocus (4.3)
X-ray tube	Tube manufacturer	X-ray WorX	Excillum	Comet
	Tube model	XWT-190-TCNF Plus	Nanotube N2	MXR-225MF
	Target type	Transmission	Transmission	Reflection
	Acceleration (maximum)	100 kV (190 kV)	60 kV (110 kV)	140 kV/100 kV (225 kV)
	Target power	1 W–10 W	0.2 W–2.1 W	50 W–200 W
	Nominal focal spot sizes	1.2 μm–10 μm[a]	0.3 μm–1.0 μm[a]	50 μm–200 μm[b]
	Filter	None	None	1 mm copper
Detector	Detector manufacturer	Perkin Elmer	DirectConversion	Varian
	Detector model	XRD 1611 CP3	XC-Actaeon	1308 DX
	Principle	CsI scintillator	Photon counting CdTe	DRZ+ scintillator
	Pixel matrix	4096 × 4096	256 × 256	640 × 1024
	Pixel pitch (SR$_b$)	100 μm (104 μm)	100 μm (N/A)	127 μm (140 μm)
	Source-detector distance	1400 mm	660 mm	1000 mm
	Nominal magnification	540×–220×	960×	14×
Aperture	Gauge manufacturer	CARY	zoneplates.com	—
	Type	Ring gauge	Custom calibration chart	ASME Penny
	Material	Tungsten carbide	Tungsten	Stainless steel
	Aperture diameter	100 μm	10 μm	1.51 mm
	Thickness	100 μm	1.6 μm	1.51 mm
Method	Type	Line pair gauge	E-beam characterisation	Pinhole imaging
	Comparison to focal spot reconstruction	Modulation transfer function (MTF) on line pair gauge JIMA RT RC-02B	Derived from measurement of e-beam diameter and simulation of electron diffusion in target	Pinhole Ø 13 μm, 50 μm thickness, magnification 25× (according to ASTM 1165-20)

[a] Focal spot size is approximated by 2 times the specified resolution.
[b] Focal spot size according to ASTM 1165-12.

simulations were performed using aRTist 2.10 [22]. A point x-ray source was placed in front of tungsten carbide aperture gauges of different thicknesses and diameters, leading to different edge transmission angles, i.e. half-cone beam angles. The SOD was 1 mm and the SDD 1000 mm, resulting in a geometric magnification of 1000× and an effective pixel size of 0.1 μm. An acceleration voltage of 100 kV on a 2 μm thick tungsten transmission target was simulated, with a corresponding average x-ray energy of 29.7 keV. A 2 μm FWHM focal spot was introduced by convoluting the simulated radiographs with a 2D Gaussian profile in ImageJ [23]. Subsequently, the simulated aperture radiographs were evaluated using focal spot reconstruction. To render the simulation results comparable, equation (6) was normalised to the nominal focal spot size *a*:

$$u_{\mathrm{rel}}(\%) = \frac{\sqrt{a^2 + u^2}}{a} - 1. \qquad (8)$$

Figure 5(b) shows the results from the radiographic simulations in comparison to the linearised model. Approximating $t_{\mathrm{x\text{-}ray}}$ by the penetration depth, where 90% of the intensity is absorbed, led to good agreement between the two. Thus, it is defined by $t_{\mathrm{x\text{-}ray}} = -\ln(0.1)/\mu_E$, where μ_E is the material and energy dependent x-ray absorption coefficient in mm^{-1}, at the weighted average energy of the x-ray spectrum. In this case, the absorption coefficient of tungsten carbide $\mu_{29.7\mathrm{keV}} = 33.3 \ \mathrm{mm}^{-1}$ led to an apparent radiographic thickness of $t_{\mathrm{x\text{-}ray}} = 0.07$ mm. Since the model assumes linear

absorption in the gauge material, it is only valid for thin gauges and reasonably small transmission angles. It is, however, a worst-case estimation of the blur by edge penetration. Thus, setting the tolerable blur at 5% of the focal spot FWHM, the following inequality for the effective gauge thickness was formulated:

$$t_{\mathrm{eff}} \leqslant \frac{0.64 \, a \, \mathrm{SDD}}{md}. \qquad (9)$$

For the cases simulated in figure 5(b), the critical effective gauge thicknesses were 0.013 mm (Ø 100 μm), 0.026 mm (Ø 50 μm), and 0.064 mm (Ø 20 μm), corroborating that the deviations remained below 5 %.

4. Experimental validation of focal spot reconstruction

To validate the focal spot reconstruction method experimentally, it was compared to complementary methods for focal spots ranging from 0.3 μm to 200 μm (FWHM). To cover this range, three different x-ray tubes, featuring transmission and reflection type targets, measurement setups and gauges shown in table 1 were used. The complementary methods included comparison to line pair gauges (JIMA) for microfocus, e-beam characterisation for submicrofocus, and pinhole camera imaging for mesofocus focal spots.

4.1. Microfocus spots compared to line pair gauge

A microfocus x-ray tube (XWT-190-TCNF Plus, x-ray WorX), with a maximum acceleration voltage of 190 kV and nominal focal spot sizes down to 1 μm, was used in combination with a custom tungsten carbide ring gauge (CARY) with a nominal diameter of 100 μm and a thickness of 100 μm (table 1). Radiographs of the ring gauge and a JIMA line pair gauge (JIMA RT RC-02B) were recorded at 100 kV using different powers and operating modes. Three spot sizes, ranging from 1 μm to 10 μm FWHM, were realised by operating the x-ray tube in different modes at different target powers: nanofocus at 1 W, microfocus at 5 W, and high-power at 10 W. To ensure similar focal spot conditions, the gauges were measured shortly after each other without switching off the x-ray tube.

The radiographs of the JIMA target were analysed in ImageJ [23]. Depending on the resolution, between 150 and 400 profiles were integrated to improve the CNR. The profiles were corrected with a linear baseline to account for grey value gradients. Subsequently, the modulation transfer function (MTF) was determined according to MTF = $(a − b)/(a + b)$, with the parameters defined in figure 6(e). It is emphasised that this definition is only applicable to grid structures with equivalent gap and line widths. To estimate the uncertainty of the JIMA derived MTF, the specified manufacturing tolerance of the line widths, ranging from 8% to 10% depending on structure size, and 5% uncertainty on the MTF value, estimated from noise and repeatability, were taken into account. To compare the reconstructed x-ray focal spots, they were convoluted with the image of a synthetic line pair gauge and analysed in the same way as the radiographs of the line pair gauge (figure 6).

Figures 7(a)–(c) shows reconstructed microfocus spots in a range from 1 μm to 10 μm FWHM, all displaying a radially symmetrical intensity distribution. The comparison of the MTF numerically calculated from the reconstructed focal spot image and measured from a line pair gauge (JIMA target), is shown in figures 7(d)–(f). The reason that the MTF did not converge to 100% is attributed to a larger secondary focal spot, i.e. parasitic radiation originating from structures within the x-ray tube, which are hit by secondary electrons (refer to [24] for details). The MTF values for the 2.6 μm and 7.4 μm focal spot agreed well for both methods (figures 7(e) and (f)). The underestimation of the MTF for the smallest focal spot (1.5 μm, figure 7(d)) is attributed to edge penetration of the relatively thick (100 μm) aperture. According to equation (7), the effective thickness of the used gauge was 0.06 mm, calculated using the penetration length of tungsten carbide $t_{x\text{-ray}} = 0.07$ mm, at the mean weighted x-ray energy of 29.7 keV, and the actual gauge thickness of $t_{gauge} = 0.1$ mm. The maximum permissible effective gauge thickness of 0.02 mm (equation (9) using a spot size of 1.5 μm), was greatly exceeded, whereas the ones for the 2.6 μm and 7.4 μm spots were compatible (0.07 mm and 0.3 mm, respectively). This indicates that the thickness of the employed ring gauge currently limits the minimum measurable spot size to about 2 μm at a magnification of 300×. This can be overcome, however, by using thinner gauges as shown in the next section.
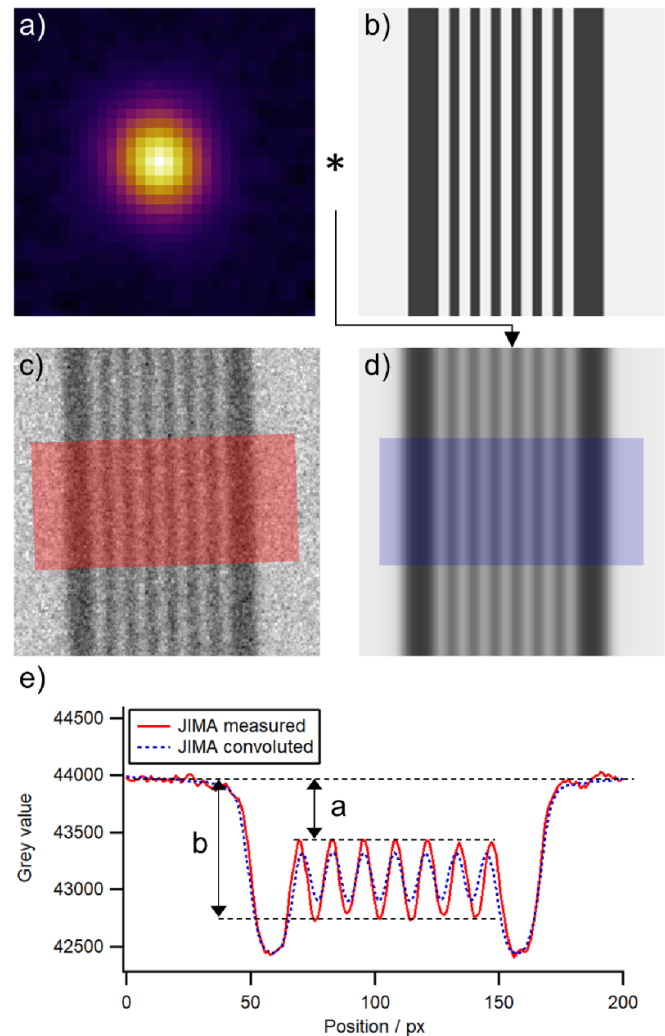

Figure 6. To compare a reconstructed focal spot (a) to radiographs of a JIMA line pair gauge (c), it is convoluted with a synthetic line pair gauge (b) resulting in (d). The resulting modulation transfer function (MTF) is compared using averaged line profiles (e).

4.2. Sub-microfocus spots compared to e-beam characterisation

To validate the method for focal spots below 1 μm, an Excillum Nanotube N2 was used in combination with a Ø 10 μm aperture in a 1.6 μm thick tungsten layer (table 1). As a complementary method, the e-beam diameter was characterised employing a structured target. To account for electron diffusion in the target material, an expansion factor, determined from simulations, was added to the e-beam diameter to estimate the x-ray focal spot size. A rough estimate put the uncertainty of the method at about 0.1 μm. From radiographs of the Ø 10 μm aperture, focal spots were reconstructed. Figures 8(a) and (b) show two examples with a FWHM of 0.32 μm and 0.54 μm. Figure 8(c) shows the comparison between the e-beam characterisation and the focal spot reconstruction. The reconstruction systematically underestimated the focal spot size, however, deviations did not exceed 0.11 μm. The standard deviations over three measurements were within 20 nm indicating high consistency of the focal spot reconstruction
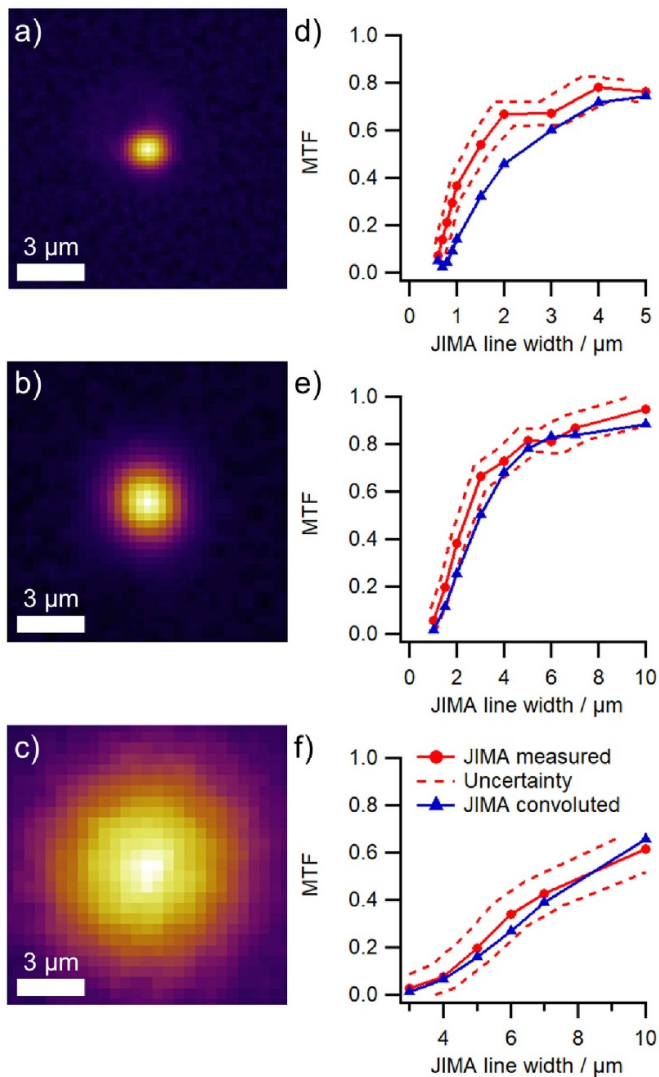
Figure 7. Reconstructed focal spots of a microfocus x-ray source with FWHM of 1.5 μm (a), 2.6 μm (b), and 7.4 μm (c) deduced from radiographs of a Ø 100 μm aperture. (d)–(f) MTF comparison between a measured JIMA line pair gauge (JIMA measured) and the reconstructed focal spot convoluted with a synthetic line pair gauge (figure 6).
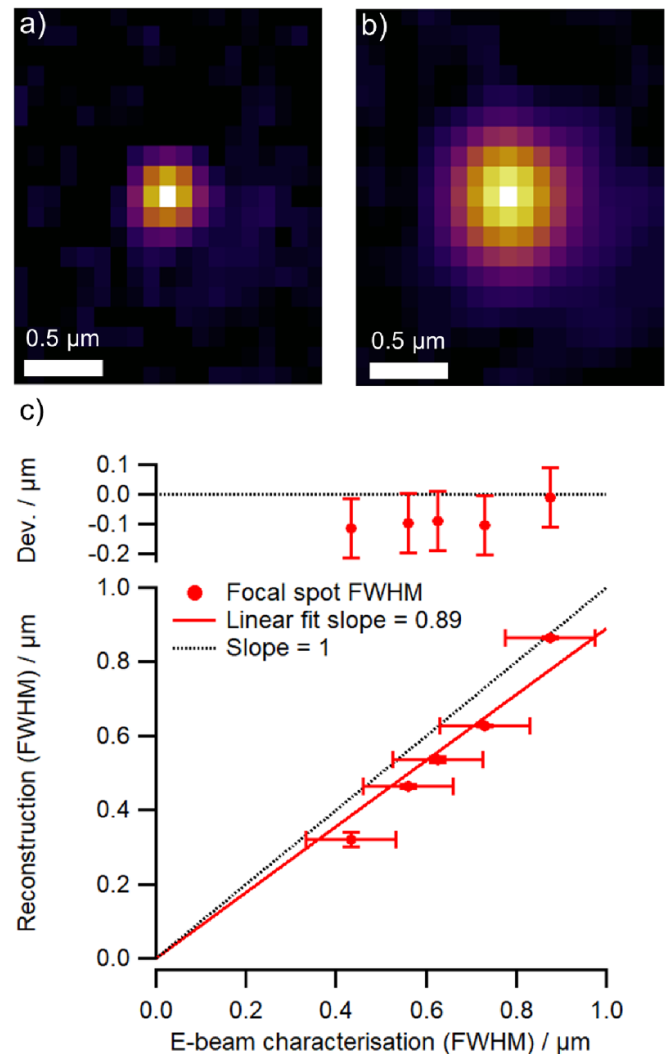
Figure 8. Reconstructed focal spots of a sub-microfocus x-ray source with FWHM of 0.32 μm (a) and 0.54 μm (b) from a Ø10 μm aperture. (c) Comparison to focal spot sizes derived from e-beam characterisation. Errors bars represent the standard deviation of three measurements (vertical) and the estimated uncertainty of the e-beam characterisation (horizontal). The inset shows the deviations (Dev.).

and stability of the x-ray tube. Since no traceable calibration of the diameter of the used aperture was available, no further conclusions can be drawn. A calibration of the aperture diameter is likely to reduce the scale error, which was about 11%. In conclusion, the focal spot reconstruction method is applicable to map the intensity distribution of focal spots with FWHM of a few 100 nm.

4.3. Mesofocus spots compared to pinhole imaging

To ensure comparability with pinhole measurements, a Comet MXR-225MF mesofocus x-ray tube with nominal focal spot sizes ranging from 50 μm to 200 μm was used in combination with a Ø 1.51 mm aperture (table 1). Figures 9(a)–(c) shows the pinhole images and figures 9(d)–(f) the reconstructed focal spots at different target powers. The nominal magnification for pinhole imaging was 25× and for reconstruction 14×.

The FWHM of both methods agreed within the uncertainty (figure 9(g)), which was estimated assuming a 2% scale error, as a result of deviations in the geometrical arrangement, and a contribution from pinhole edge penetration according to ASTM 1162-20, Note 1. In terms of resolution, pinhole imaging is favourable for larger spot sizes, however, for smaller focal spots (<50 μm) it seems to overestimate the focal spot size due to blur introduced by pinhole edge penetration.

5. Routes towards traceability

A traceable calibration of the aperture is key to achieve accurate and comparable measurements. First, the aperture diameter is used as a scale reference to derive the effective pixel size, i.e. the magnification. Second, the aperture form deviations need to be considered in the uncertainty estimation of the focal spot reconstruction method. The advantage of using
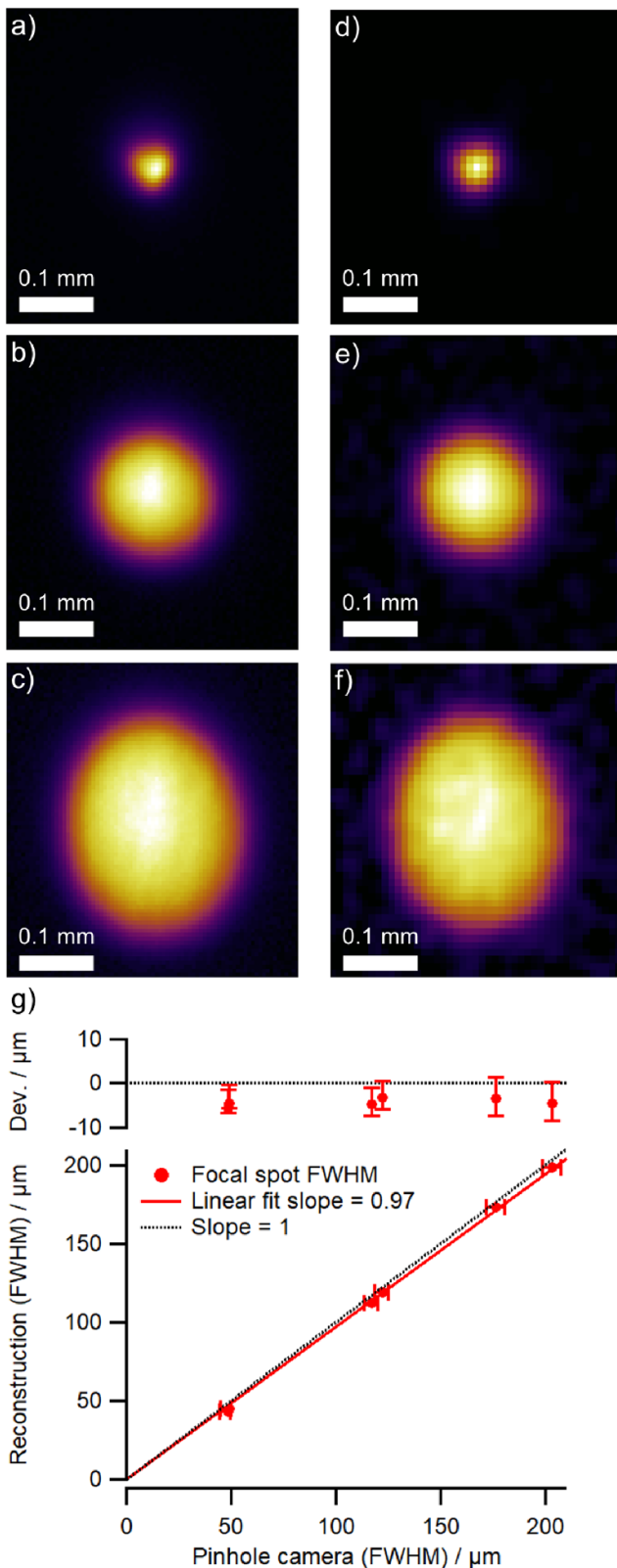
Figure 9. Focal spot distributions of a mesofocus x-ray tube from pinhole imaging (a)–(c) and reconstruction from a Ø 1.5 mm aperture (d)–(f). (g) Comparison of reconstruction to pinhole camera imaging. Error bars represent the uncertainty due to scale errors and pinhole edge penetration. The inset shows the deviations (Dev.).

circular aperture structures is that they are fully characterised by their diameter and roundness deviation, assuming a negligible thickness.

Diameter and form deviations of the tungsten carbide ring gauge (CARY) with a nominal diameter and thickness of 100 μm, were determined on a tactile μ-coordinate measuring machine [25] with an expanded measurement uncertainty of 0.10 μm. Nine circular profiles along the cylinder axis with a vertical spacing of 10 μm were scanned. The average diameter was 100.18 μm and the maximum roundness deviation 0.26 μm. From figure 4(d) we derive that such roundness deviation affects the FWHM of a 1 μm focal spot by less than 3%, however, the thickness of the gauge limits the focal spot size to be measured to above 2 μm due to edge penetration (equation (9)).

Traceable calibration of thin, micro-fabricated structures used for sub-microfocus spot reconstruction (section 4.2) is more challenging. Optical and scanning probe microscopy techniques are required, however, the former is limited in accuracy and the latter is extensive and time consuming.

6. Conclusion and outlook

We presented a method to image the 2D intensity distribution of x-ray focal spots ranging from sub-microfocus (0.1 μm) to mesofocus (>50 μm). It uses the edge blur of a circular aperture to reconstruct the focal spot using filtered back projection. The aperture diameter is thereby used as a scale reference. Different influence factors, such as image noise, aperture form deviations and edge penetration, were quantified using simple analytical models and simulations. They enabled us to propose boundary conditions and estimate an initial measurement uncertainty for the focal spot reconstruction. Thus, measurements can be rendered traceable by using a calibrated aperture. The boundary conditions were defined in such a way that the expanded uncertainty does not exceed 10%. For a more accurate estimation of the uncertainty, more sophisticated radiographic simulations are required.

The focal spot reconstruction method has been validated experimentally against e-beam characterisation for sub-microfocus spots, line pair gauges (JIMA target) for microfocus spots, and pinhole imaging for mesofocus spots. Good agreement was achieved when complying with the boundary conditions. For spots <50 μm it is recommended to use focal spot reconstruction instead of pinhole imaging, since pinhole edge penetration starts to significantly influence the results. Limitations of the method include that it requires a high CNR in the aperture radiographs, and highly accurate and thin gauges.

To cover a wide focal spot range, it is suggested to manufacture an aperture gauge with a thickness below 10 μm made from a high-density material, such as gold or tungsten. It should feature aperture diameters from about 10 μm to 500 μm to comply with the boundary conditions, which specify the measurement parameters in a way to avoid adverse effects,

such as edge penetration or insufficient resolution. We expect that when using such a gauge, expanded measurement uncertainties of about 3% can be achieved. Further work is required to render traceable reference calibration of micro-structured gauges more efficient.

Data availability statement

The data that support the findings of this study are openly available at the following URL/DOI: https://doi.org/10.5281/zenodo.6461222.

An open-access implementation of the x-ray focal spot reconstruction method is available as part of NxS Tool (NxS Tool: Measurement of the focal spot size and shape for micro- and nano- focus x-ray generators, Université Paris-Saclay, CEA, List, F-91190, Palaiseau, France, distributed by CEA LIST (http://www-list.cea.fr/en/) at https://nanoxspot-project.cea.fr/).

Acknowledgments

ORCID iDs

Benjamin A Bircher ● https://orcid.org/0000-0002-1494-6732
Felix Meli ● https://orcid.org/0000-0001-7575-7540

References

[1] Uhlman N, Salamon M and Burtzlaff S 2008 Components and methods for highest resolution computed tomography *Int. Symp. NDT Aerospace December* vol **1** (*Fürth, Germany*) pp 3–9

[2] Fleßner M, Vujaklija N, Helmecke E and Hausotte T 2014 Determination of metrological structural resolution of a CT system using the frequency response on surface structures *Proc. MacroScale* pp 1–10

[3] Illemann J 2020 Traceable measurement of the instrument transfer function in dXCT *10th Conf. on Industrial Computed Tomography* (*Wels, Austria*) pp 1–7

[4] Arenhart F A, Baldo C R, Fernandes T L and Donatelli G D 2016 Experimental investigation of the influencing factors on the structural resolution for dimensional measurements with CT systems *6th Conf. on Industrial Computed Tomography* (*Wels, Austria*) pp 1–12

[5] Weiß D, Shi Q and Kuhn C 2012 Measuring the 3D resolution of a micro-focus x-ray CT setup *4th Conf. on Industrial Computed Tomography* (*Wels, Austria*) pp 1–9

[6] Rueckel J, Stockmar M, Pfeiffer F and Herzen J 2014 Spatial resolution characterization of a x-ray microCT system *Appl. Radiat. Isot.* **94** 230–4

[7] Zanini F and Carmignato S 2017 Two-spheres method for evaluating the metrological structural resolution in

[8] Jobst A, Kostka G and Schmitt P 2004 Neue Methode zur Charakterisierung von Brennflecken kleiner als 5 μm *German Society of NDT - Jahrestagung* (*Salzburg*)

[9] Fry D, Ewert U, Gollwitzer C, Neuser E and Selling J 2012 Measuring microfocal spots using digital radiography *Mater. Eval.* **70** 981–90

[10] Salamon M, Hanke R, Krüger P, Sukowski F, Uhlmann N and Voland V 2008 Comparison of different methods for determining the size of a focal spot of microfocus x-ray tubes *Nucl. Instrum. Methods Phys. Res.* A **591** 54–58

[11] Baier M, Zanini F, Savio E and Carmignato S 2018 A new conversion approach between different characterization methods to measure the spot size of micro computed tomography systems *European Society for Precision Engineering and Nanotechnology, Conf. Proc.—18th Int. Conf. and Exhibition, EUSPEN 2018* pp 445–6

[12] Illemann J, Meinel D and Bellon C 2019 Effektive Bestimmung der Fokusparameter von Mikrofokus-Röntgenquellen *DGZfP Jahrestagung* (*Friedrichshafen, Germany*)

[13] Bavendiek K, Ewert U, Riedo A, Heike U and Zscherpel U 2012 New measurement methods of focal spot size and shape of x-ray tubes in digital radiological applications in comparison to current standards *18th World Conf. on Nondestructive Testing* (*Durban, South Africa*)

[14] Di Domenico G, Cardarelli P, Contillo A, Taibi A and Gambaccini M 2016 X-ray focal spot reconstruction by circular penumbra analysis—application to digital radiography systems *Med. Phys.* **43** 294–302

[15] Probst G M, Hou Q, Boeckmans B, Xiao Y S and Dewulf W 2020 Characterization and stability monitoring of x-ray focal spots *CIRP Ann.* **69** 2–5

[16] Russo P and Mettivier G 2011 Method for measuring the focal spot size of an x-ray tube using a coded aperture mask and a digital detector *Med. Phys.* **38** 2099–115

[17] Engelhardt M and Baumann J 2006 Determination of size and intensity distribution of the focal spot of a microfocus x-ray tube using image processing *9th European Conf. on NDT* (*Berlin, Germany*) pp 1–13

[18] Peng W, Xiao Y and Hou Q 2019 Focal spot intensity distribution estimation of x-ray tube via machine learning *Int. Symp. Digital Industrial Radiology and Computed Tomography—DIR20192* (*Fürth, Germany*) pp 1–8

[19] Kak A C and Slaney M 2001 *Principles of Computerized Tomographic Imaging* (Philadelphia, PA: Society for Industrial and Applied Mathematics) (https://doi.org/10.1137/1.9780898719277)

[20] Srinivasan K, Mohammadi M and Shepherd J 2014 Investigation of effect of reconstruction filters on cone-beam computed tomography image quality *Australas. Phys. Eng. Sci. Med.* **37** 607–14

[21] Bechara B, McMahan A C, Moore W S, Noujeim M, Geha H and Teixeira B F 2012 Contrast-to-noise ratio difference in small field of view cone beam computed tomography machines *J. Oral Sci.* **54** 227–32

[22] Bellon C, Deresch A, Gollwitzer C and Jaenisch G-R 2012 Radiographic simulator aRTist: version 2 *18th World Conf. Nondestructive Testing* (*Durban, South Africa*)

[23] Schindelin J *et al* 2012 Fiji: an open-source platform for biological-image analysis *Nat. Methods* **9** 676–82

[24] Boone M N, Vlassenbroeck J, Peetermans S, Van Loo D, Dierick M and Van Hoorebeke L 2012 Secondary radiation in transmission-type x-ray tubes: simulation, practical issues and solution in the context of x-ray microtomography *Nucl. Instrum. Methods Phys. Res.* A **661** 7–12

[25] Küng A, Meli F and Thalmann R 2007 Ultraprecision micro-CMM using a low force 3D touch probe *Meas. Sci. Technol.* **18** 319–27